APPLICATION NOTE

Model 110 Automatic Twin-Jet Electropolisher
Model 1040 NanoMill® TEM specimen preparation system

The role of TEM specimen preparation in understanding aluminum alloy precipitation hardening mechanism

Precipitation hardening is the most widely used process for improving the mechanical properties of aluminum alloys. The ability to target a region of interest on conventionally prepared specimens using the NanoMill system resulted in TEM specimens of high-quality and thickness that were suitable for high resolution TEM and aberration-corrected STEM imaging and analysis.

Aluminum alloys are widely used in the aerospace industry due to the alloys' low density, light weight, and high strength [1]. Precipitation (or age) hardening is the most widely used process for improving the mechanical properties of aluminum alloys AA2xxx, AA6xxx, and AA7xxx. Historically, age hardening was recognized in Al -4% Cu alloy, which is the best example to describe the precipitation hardening phenomenon. Al -4% Cu alloy at equilibrium and at room temperature consists of two phases: matrix α (aluminum) and intermetallic phase θ (Al_2Cu). The process of precipitation hardening involves three steps:

1. **Solution treatment**. Alloy is heated above the solvus temperature (550 °C) to obtain a homogeneous, solid solution of copper atoms in the aluminum matrix - α phase.
2. **Quenching**. α solid solution is quenched fast enough that the θ phase does not precipitate; the Cu atoms remain in solution α in excess, thus forming the supersaturated, solid solution α_{SS}.
3. **Aging**. α_{SS} is heated below the solvus temperature to produce finely dispersed precipitates.

In the initial period of the aging process, the atoms of copper disperse in the α_{SS} solution cluster in local groups and form regions called Guinier-Preston (GP) zones. The GP zones nucleate homogeneously in the matrix and are coherent with the matrix. With increased aging time, transformation of GP zones into θ'' particles occurs. The θ'' particles, like the GP zones, are coherent with the matrix. The precipitates, like the GP zones, strengthen the alloy. The next intermediate phase, θ', is semi-incoherent within the matrix. The formation of θ' precipitates decrease the alloy's hardness. The stable θ (Al_2Cu) phase nucleates at the interface: matrix grain boundaries / θ'. The alloy strengthening is caused by the interaction of dislocations surrounding small and coherent precipitates.

The aging process for Al -4% Cu alloy can be described as follows:

$$\alpha_{SS} \rightarrow \alpha_1 + \text{GP zones} \rightarrow \alpha_2 + \theta'' \rightarrow \alpha_3 + \theta' \rightarrow \alpha_4 + \theta$$

In more complex alloys, such as AA2xxx, AA6xxx, and AA7xxx, the low temperature precipitation processes are intricate and the precipitation sequence and compositions depend on alloy composition and aging temperature.

Electron microscopy has elucidated the structure and morphology of the stable precipitates in aluminum alloys [2-8]. However, GP zones and metastable precipitates are difficult to characterize due to their small size – less than 3 nm [5, 9-11]. Although the transition from the metastable to stable precipitates for the aluminum alloys above is well known, the mechanisms of formation are not well understood. Understanding the precipitation hardening mechanism is critical for the development of new alloys or thermal processes. With the advent of aberration-corrected microscopes, characterization of the GP zones and meta-stable precipitates – elemental distribution and orientation – is now feasible and enables the identification of the transition mechanisms for precipitate

evolution. High-angle annular dark field scanning transmission electron microscopy (HAADF-STEM) imaging is a straight-forward characterization for elemental distribution and identification with the intensity, *I,* being dependent on the atomic number, Z, of the specimen: $I = Z^{\alpha}$ where $\alpha = 1.2 \sim 2$ [12-15]. For aberration-corrected HAADF-STEM imaging and analysis, specimen thickness of 50 to 20 nm or less is imperative [16].

This application note presents specimen preparation of two aluminum alloys, AA7050 and AA2050, which result in a specimen thickness suitable for aberration-corrected scanning transmission electron microscopy (AC-STEM) imaging and analysis. Traditional electropolishing and concentrated Ar ion beam milling techniques were both employed to elucidate the GP zones and meta-stable precipitates in aluminum alloys. This application note is extracted from research on precipitation mechanisms in AA7050 [17] and AA2050 [18] performed by Tsai-Fu Chung at the Department of Materials Science and Engineering, National Taiwan University, Taiwan.

Materials and specimen preparation

Two aluminum alloy systems were investigated:

- **AA7050**: Al-6.25Zn-2.14Mg-2.23Cu-0.05Fe-0.03Si (wt.%), and
- **AA2050**: Al-3.6Cu-0.9Li-0.34Mg-0.35Ag-0.34Mn-0.08Zr (wt.%).

Details of the alloys' heat treatments and ageing process are described in [17] and [18], respectively.

TEM specimens 3 mm in diameter were prepared from bulk specimens by cutting and mechanical thinning to a thickness of 70 µm. The discs were then electropolished using the Model 110 Automatic Twin-Jet Electropolisher [Fischione Instruments]; a concentrated Ar ion beam milling system, the Model 1040 NanoMill® TEM specimen preparation system [Fischione Instruments] (Figure 1) was used to remove surface oxides from electropolishing and to further reduce specimen thickness (Figure 2). During Ar ion milling, a concentrated beam of less than 1 µm in size was rastered across the targeted area on the specimen. Table 1 summarizes the electropolishing and Ar ion milling conditions for each processed alloy.

Figure 1. Model 110 Automatic Twin-jet Electropolisher and Model 120 Automatic Power Control (top). Model 1040 NanoMill® TEM specimen preparation system (bottom).

Table 1. TEM specimen preparation conditions for AA7050 and AA2050 aluminum alloys.

	Specimen preparation conditions	
Specimen preparation instrument	AA7050 Al alloy	AA2050 Al alloy
Model 110 Automatic Twin-Jet Electropolisher	• 33% nitric acid/ 67% methanol solution • -20 °C • 10 V	• 33% nitric acid/ 67% methanol solution • -25 °C • 12 V
Model 1040 NanoMill® TEM specimen preparation system	• 900 eV, 100 pA, ±10° specimen tilt, 20 min per side • 500 eV, 100 pA, ±10° specimen tilt, 30 min per side	

High resolution transmission electron microscopy (HRTEM) and aberration-corrected high angle annular dark field scanning transmission electron microscopy (HAADF-STEM) imaging and analysis were performed on the formed precipitates using a TEM [Thermo Fisher Scientific] operated at 200 kV. HAADF-STEM imaging, which is highly sensitive to atomic number (Z), was performed to differentiate the atomic structure of the precipitates in the aluminum alloys.

Results and discussion

Evolution of precipitates in AA7050

The evolution of the precipitates at edge-on configurations were observed along the $[110]_{Al}$ zone axis in the TEM. Because the bulk specimens were exposed to a creep-age forming step, only GPII zones, η' and η were observed on the Al matrix. The precipitate evolution is as follows:

$$\alpha_{SS} \rightarrow \text{GPII} \rightarrow \eta' \text{ precipitates} \rightarrow \eta \text{ precipitates}$$

To accurately identify the precipitates, analysis of the fast Fourier transform (FFT) diffractograms on the observed precipitates was performed on the HRTEM and HRSTEM images. The FFT diffractograms were compared to simulated diffraction patterns for each precipitate type on the $[110]_{Al}$ zone axis. Figure 3 are HRTEM images of representative areas of the analyzed precipitates. The GPII zone in Figure 3 is only a few atomic

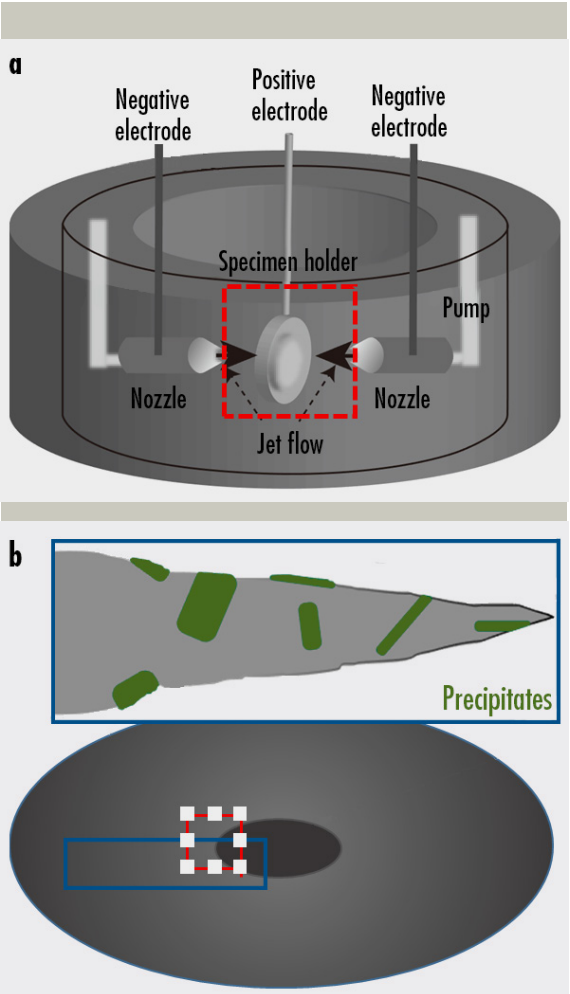

Figure 2. Specimen preparation of the 3 mm aluminum alloys by electropolishing (a) followed by concentrated ion beam milling (b) for further specimen thinning. The red raster box (b) at the perforated area of the specimen corresponds to the targeted area during ion milling. Inset (b) is a cross section of the specimen showing the thin region of the wedge-shaped specimen.

layers on the $(1\bar{1}1)_{Al}$ habit plane. The GPII zones , η' and η were measured as 3 to 5 nm, 5 to 10 nm, and 5 to 30 nm in size, respectively.

Four variants of η' can evolve to 11 types of η with the morphology and orientation relationships well known for both types of precipitates. The mechanisms for the evolution of 4 to a possible 11 variants of precipitates are of interest and require

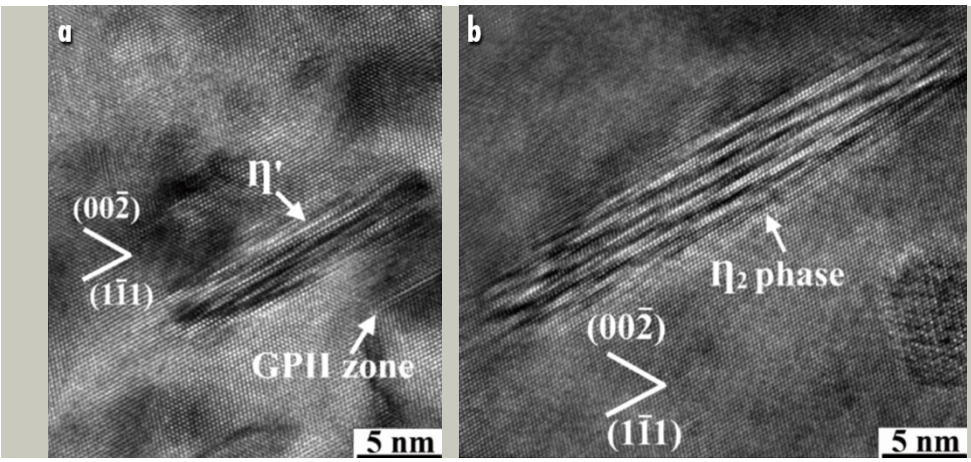

Figure 3. High resolution transmission electron microscopy images on the [110] zone axis of Al with GPII zone and η' (a) and η_2 (b) precipitates identified.

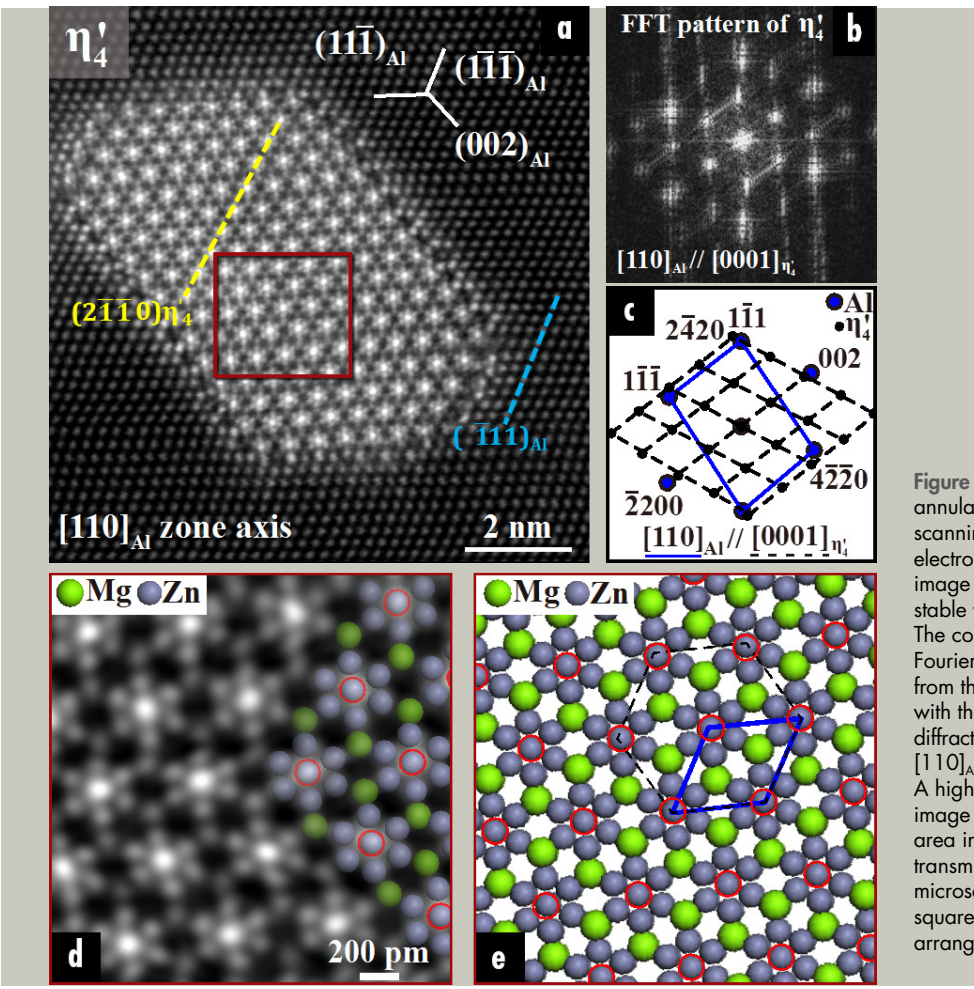

Figure 4. High-angle annular dark field scanning transmission electron microscopy image (a) of the metastable η'_4 precipitate. The corresponding fast Fourier transform (b) from the image matches with the simulated diffraction pattern (c) for $[110]_{Al}$ // $[0001]\eta'_4$. A high-magnification image (d) of the marked area in the scanning transmission electron microscopy image (a, red square) shows the hexad arrangement (d, e).

fundamental understanding. Chung et al. [17] has shown through in situ TEM studies that the transformation mechanism of precipitates by the simultaneous separated nucleation of η' as adjacent GPII zones dissolves. Only η_4' and η_2 are discussed in this application note.

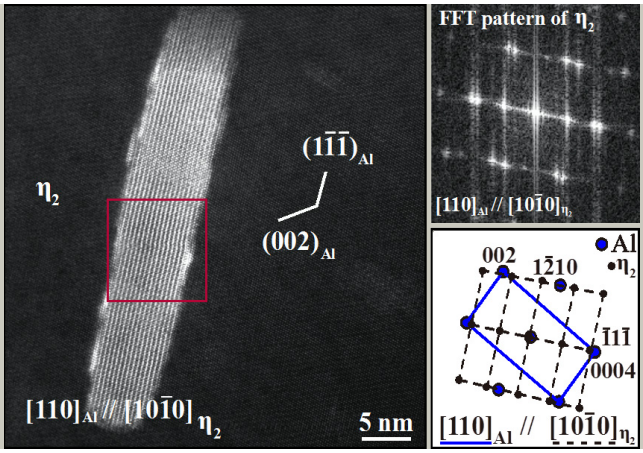

Figure 5. High-angle annular dark field scanning transmission electron microscopy image of the stable η_2 precipitate (left). The corresponding fast Fourier transform (top right) from the image matches with the simulated diffraction pattern (bottom right) for $[110]_{Al}$ // $[10\bar{1}0]\eta_2$.

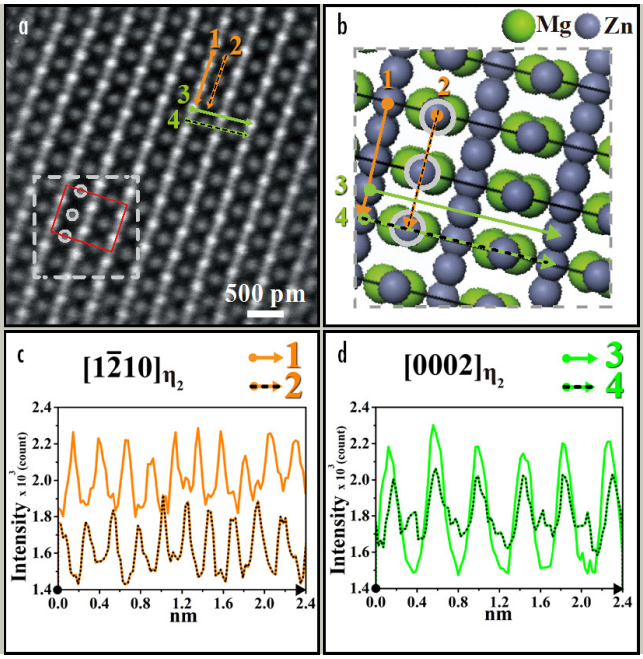

Figure 6. A high-magnification image (a) of the marked area in Figure 5 (red square) showing the atomic distribution of Mg and Zn. This atomic distribution was modeled (b). Line profiles 1,2 (c) and 3,4 (d) were extracted in the $[1\bar{2}10]$ and [0002] direction, respectively, showing the variation in intensities.

The meta-stable η_4' precipitate was differentiated from the η_4 precipitate by the $(2\bar{1}\bar{1}0)\eta'_4$ facet being non-parallel with the $(\bar{1}11)$ plane of Al (Figure 4). The HAADF-STEM image of the η_4' precipitate shows a hexad arrangement of the atoms (atomic model and HAADF-STEM image in Figure 4). This hexad is comprised of the high intensity atom Zn (gray ball with red circle) surrounded by six Zn atoms (gray balls) of slightly lower intensity, which are bonded to the lowest intensity atoms of Mg (green balls). The evolution of the η_4' precipitate was determined as a result of the coalescence of two precipitates.

The η_2 precipitate was easily found throughout the specimen during HRTEM imaging. For the same $[110]_{Al}$ zone axis, the stable η_2 precipitate was found to be larger in size when compared to η'_4 precipitate (Figure 5). Intensity fluctuations on the η_2 precipitate was observed; this is attributed to the sandwiched stacking structure within the precipitate under the $[110]_{Al}$ zone axis.

Figure 6a is a high-magnification image of the marked area in Figure 5. At this magnification, the atomic positions based on the highest and lowest intensities for Zn and Mg (gray and

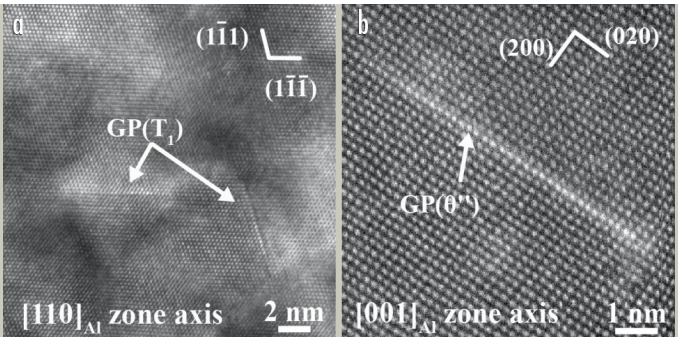

Figure 7. A high-resolution transmission electron microscopy image (a) acquired on the $[110]_{Al}$ zone axis showing two GP(T_1). A high angle annular dark field scanning transmission electron microscopy image (b) acquired on the $[001]_{Al}$ zone axis showing a GP(θ'').

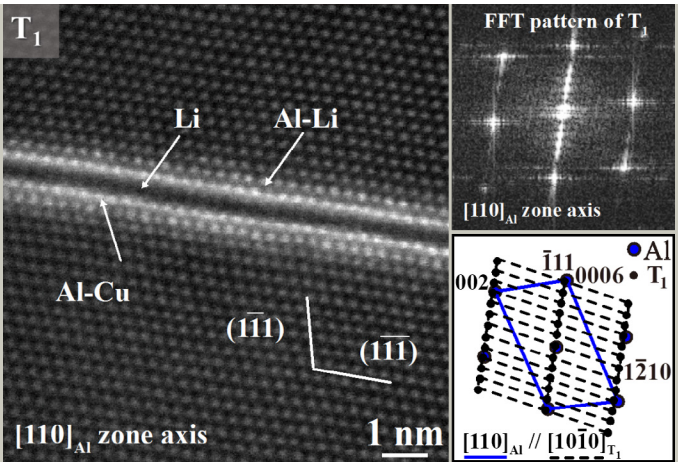

Figure 8. High angle annular dark field scanning transmission electron microscopy image (left) of a T_1 precipitate along the (1$\bar{1}\bar{1}$) of Al acquired along the $[110]_{Al}$ zone axis. A corresponding fast Fourier transform pattern (top right) from the image shows correlation with a simulated diffraction pattern (bottom right) based on the orientation relationship of $[110]_{Al}$ // $[10\bar{1}0]_{T1}$.

green balls in the model), respectively, on the η_2 precipitate are determined. The labeled gray area in Figure 6a is represented in the atomic model (Figure 6b).

Line profiles 1,2 from the [1$\bar{2}$10] direction (Figure 6c) and 3,4 from [0002] direction (Figure 6d) of the η_2 precipitate were extracted from the HAADF-STEM image and are represented on the atomic model in Figure 6b. The brightest intensities are attributed to two superimposed Zn atoms, medium intensity from one Zn atom, and the lowest intensities from Mg atoms. In the [1$\bar{2}$10] direction (Figure 6c), line profile 1 consists of an array of:

Zn, two Zn, Zn, two Zn, Zn, etc.,

while line profile 2 is an array of:

Zn, vacancy, Zn, vacancy, Zn, etc.

The presence of two Zn atoms is projected on Line profile 1 with a slightly wider peak when compared to a single Zn atom, which indicates the intensity from two atoms. In the [0002] direction (Figure 6d), line profile 3 consists of an array of:

two Zn, vacancy, two Zn, vacancy, two Zn, etc.,

while line profile 4 is an array of:

Zn, Mg, Zn, Mg, Zn, etc.

The intensity from the Mg atom is confirmed by the lower intensity in between the much higher intensity Zn (Figure 6d).

The formation of η_2 during the over-ageing stage is described as a layer by layer growth that results in sandwiched stacking structures, shown here, and zigzag stacking structures as shown in previous studies [19, 20]. From the η'_4 phase, the transformation to a stable precipitate, η_2, can be described as a step-wise process: initial coalescence or transformation of two η'_4 (or η_4) and small η_2 precipitate; formation of η_4 with hexagonal stacking and finally; to η_2 precipitate. This involved gradual development of η to η'

from the hexagonal structure with a higher level of Zn. In this case, η' and η coexisted in this given precipitate during the transition, and this transformation mechanism from η' → η can be attributed to an in situ-type nucleation [17].

Evolution of precipitates in AA2050

The evolution of precipitates in AA2050 has been shown to be dependent on the habit planes of Al. The GP zone types with Al habit planes and evolving precipitates are described in the following process:

$$\alpha_{SS} \rightarrow GP(T_1)_{\{111\}Al} \rightarrow T_1 \text{ precipitates} \quad (a)$$
$$\alpha_{SS} \rightarrow GP(\theta'')_{\{100\}Al} \rightarrow \theta' \text{ precipitates} \quad (b)$$
$$\alpha_{SS} \rightarrow GPB_{\{120\}Al} \rightarrow S \text{ precipitates} \quad (c)$$

Only the precipitate transformations of (a) and (b) will be discussed in this application note.

The TEM specimens were prepared from bulk specimens treated with one-step ageing, referred to as "peak-aging" (PA) specimens and with a creep-age forming (CAF) step specimens.

Figure 7 shows HRTEM and HAADF-STEM images of GP(T_1) and GP(θ"), respectively, on the PA specimens. The observed GP(T_1) precipitates are in edge-on configurations of $(1\bar{1}1)$ and $(1\bar{1}\bar{1})$ of Al. The GP(θ") precipitate is in edge-on configuration of (020) of Al. With HAADF-STEM imaging, a single Cu layer is observed in the GP(θ") precipitate (Figure 7b), identified by high intensity atoms (when compared to the Al matrix).

Based on Figure 7, the size of GP(T_1) and GP(θ") precipitates are about 5 to 6 nm. The precipitates evolved to a larger size of about 73 and 85 nm in length for the T_1 and θ' precipitates, respectively.

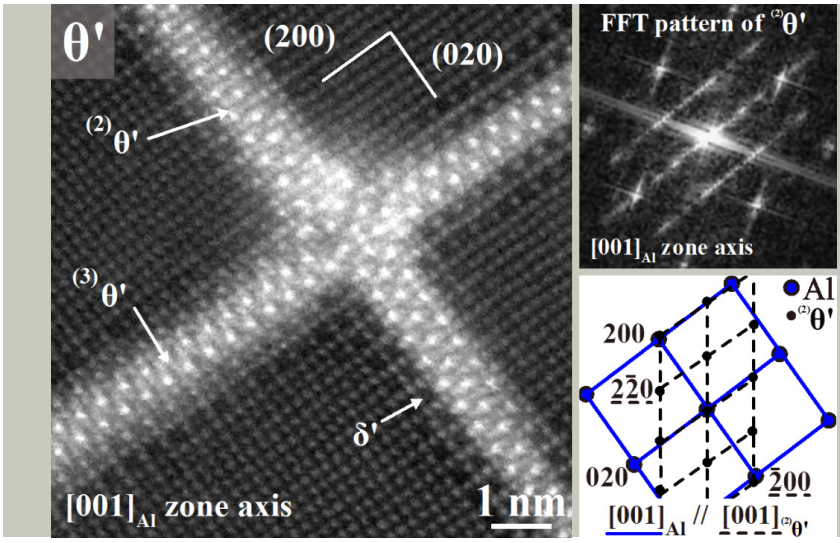

Figure 9. High angle annular dark field scanning transmission electron microscopy (HAADF-STEM) image of a θ′ precipitate acquired along the [001]$_{Al}$ zone axis of the creep-age forming specimen (left). The $^{(2)}$θ' and $^{(3)}$θ' variants of θ' precipitate bounded by δ'. A fast Fourier transform pattern (top right) from the $^{(2)}$θ' precipitate was acquired from the HAADF-STEM image and correlated to a simulated diffraction pattern (bottom right) for the orientation relationship of [001]$_{Al}$ // [001]$^{(2)}$θ'.

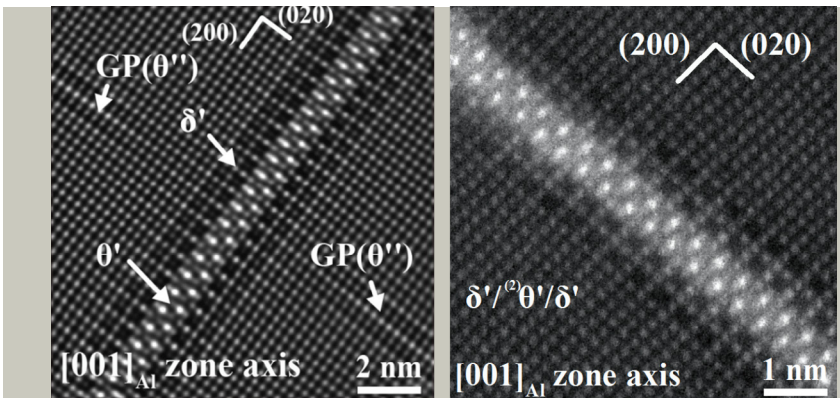

Figure 10. Processed high angle annular dark field scanning transmission electron microscopy image (left) of GP(θ"), θ′ ($^{(2)}$θ' variant), and δ' precipitates acquired along the [001]$_{Al}$ zone axis. The single Cu layer GP(θ") precipitate (left) evolves into a two Cu layers $^{(2)}$θ' precipitate with two adjacent δ' precipitates forming δ'/$^{(2)}$θ'/δ' (right).

To differentiate T_1 and θ' precipitates, analysis of the corresponding FFT from the HAADF-STEM images and atomic distribution were performed. Figure 8 shows T_1 precipitate with the corresponding FFT and simulated diffraction pattern.

The difference in intensity of the atoms provided the identification of the atomic layers of T_1 precipitate (Figure 8). The brightest intensity corresponds to a Cu-containing layer, Al-Cu in this case, with Cu of higher atomic number than Li or Al; the darkest intensity layer is Li. The slightly brighter layer of atoms corresponds to a mixture of Al-Li. This atomic arrangement for T_1 precipitate corresponds to previous work in the literature.

The investigation of θ' precipitate was performed using the CAF specimens. Along the [001] zone axis of Al, two variants of the θ' precipitate, $^{(2)}$θ' and $^{(3)}$θ', at edge configurations on the (020) and (200) planes of Al, respectively, were observed (Figure 9). This is expected because the growth of the dominant variant $^{(2)}$θ' in the (020) plane of Al is attributed to stress formation during CAF process from previous studies.

The cross-shape morphology of the θ′ precipitate (Figure 9) is a result of the simultaneous growth of $^{(2)}$θ' and $^{(3)}$θ' precipitates. The disordered atomic structure at the center joining the two variants of θ′ precipitate is probably from the strain field. Based on the HAADF-STEM (Figure 9), the center of the θ′ precipitate is comprised of high intensity atoms of Cu and bordered lower intensity atomic array containing Al-Li atoms, labelled as δ'. This atomic arrangement of δ'/θ'/δ' correlates to previous studies of the same aluminum alloy.

The microstructural evolution of GP(θ'') → θ' precipitates was determined from the PA specimens at the different areas of the specimen. The typical single Cu layer GP(θ'') can be found with θ' nearby, as is shown in Figure 10a.

From a single Cu layer in the GP(θ''), two Cu layers (highest intensity array of atoms) evolve as θ' precipitate with the repeated structure of δ'/$^{(2)}$θ'/δ' (Figure 10b). The evolution of the GP(θ'') → θ' precipitates is a diffusional growth based on in situ nucleation or transformation where the diffusion of solute atoms develops into a new precipitate of different composition and crystal structure. The growth of the θ' precipitates can be terminated by soft or hard impingement, as discussed in detail in [18].

Conclusions

TEM specimen preparation of aluminum alloys AA7050 and AA2050 by electropolishing and concentrated Ar ion milling was demonstrated. The ability to target a region of interest on conventionally prepared specimens using the NanoMill system resulted in TEM specimens of high quality and thickness suitable for HRTEM and aberration-corrected HAADF-STEM imaging and analysis. Through atomic-resolution TEM and STEM, the evolution of precipitates from GP zones, GPII for AA7050 and GP(T_1) and GP(θ'') for AA2050, meta-stable precipitates, η' for AA7050 and T_1 and θ' for AA2050; to stable precipitates, η for AA7050, was identified. The transformation of the GP zones to the meta-stable precipitates was driven by in situ nucleation during the transformation step for both alloy systems.

Acknowledgment

This application note is extracted from the doctoral thesis of Tsai-Fu Chung, Department of Materials Science and Engineering, National Taiwan University, Taipei, Taiwan.

References

[1] Nie, J. F. (2014). Physical Metallurgy of Light Alloys. In D. E. Laughlin & K. Hono (Eds.), *Physical metallurgy* (5th ed., pp. 2009-2156). Elsevier.

[2] Phillips, V. A. (1975). High resolution electron microscope observations on precipitation in Al-3.0% Cu alloy. *Acta Metallurgica*, **23**(6), 751-767.

[3] Yoshimura, R., Konno, T. J., Abe, E., & Hiraga, K. (2003). Transmission electron microscopy study of the early stage of precipitates in aged Al–Li–Cu alloys. *Acta Materialia*, **51**(10), 2891-2903.

[4] Nicholson, R. B., & Nutting, J. (1958). Direct observation of the strain field produced by coherent precipitated particles in an age-hardened alloy. *Philosophical Magazine,* **3**(30), 531-535.

[5] Chang, Y. (1992). Crystal structure and nucleation behavior of {111} precipitates in an Al-3.9Cu-0.5Mg-0.5Ag Alloy [Doctoral dissertation]. ProQuest Dissertations and Theses Global.

[6] Donnadieu, P., Shao, Y., De Geuser, F., Botton, G., Lazar, S., Cheynet, M., De Boissieu, M., & Deschamps, A. (2011). Atomic structure of T_1 precipitates in Al–Li–Cu alloys revisited with HAADF-STEM imaging and small-angle X-ray scattering. *Acta Materialia*, **59**(2), 462-472.

[7] Dwyer, C., Weyland, M., Chang, L. Y., & Muddle, B. C. (2011). Combined electron beam imaging and AB initio modeling of T_1 precipitates in Al–Li–Cu alloys. *Applied Physics Letters*, **98**(20), 201909.

[8] Duan, S., Wu, C., Gao, Z., Cha, L., Fan, T., & Chen, J. (2017). Interfacial structure evolution of the growing composite precipitates in Al-Cu-Li alloys. *Acta Materialia*, **129**, 352-360.

[9] Sha, G., & Cerezo, A. (2004). Early-stage precipitation in Al–Zn–Mg–Cu alloy (7050). *Acta Materialia*, **52**(15), 4503-4516.

[10] Berg, L., Gjønnes, J., Hansen, V., Li, X., Knutson-Wedel, M., Waterloo, G., Schryvers, D., & Wallenberg, L. (2001). GP-zones in Al–Zn–Mg alloys and their role in artificial aging. *Acta Materialia*, **49**(17), 3443-3451.

[11] Decreus, B., Deschamps, A., De Geuser, F., Donnadieu, P., Sigli, C., & Weyland, M. (2013). The influence of CU/Li ratio on precipitation in Al–CU–Li–x alloys. *Acta Materialia*, **61**(6), 2207-2218.

[12] Hartel, P., Rose, H., & Dinges, C. (1996). Conditions and reasons for incoherent imaging in STEM. *Ultramicroscopy*, **63**(2), 93-114.

[13] Bals, S., Kilaas, R., & Kisielowski, C. (2005). Nonlinear imaging using annular dark field TEM. *Ultramicroscopy*, **104**(3-4), 281-289.

[14] Krivanek, O. L., Chisholm, M. F., Nicolosi, V., Pennycook, T. J., Corbin, G. J., Dellby, N., Murfitt, M. F., Own, C. S., Szilagyi, Z. S., Oxley, M. P., Pantelides, S. T., & Pennycook, S. J. (2010). Atom-by-atom structural and chemical analysis by annular dark-field electron microscopy. *Nature*, **464**(7288), 571-574.

[15] Wang, Z. W., Li, Z. Y., Park, S. J., Abdela, A., Tang, D., & Palmer, R. E. (2011). Quantitative Z-contrast imaging in the scanning transmission electron microscope with size-selected clusters. *Physical Review B*, **84**(7), 073408.

[16] Pennycook, S. J., & Nellist, P. D. (2011). *Scanning transmission electron microscopy: Imaging and analysis* (1st ed.). Springer.

[17] Chung, T. F., Yang, Y. L., Huang, B. M., Shi, Z., Lin, J., Ohmura, T., & Yang, J. R. (2018). Transmission electron microscopy investigation of separated nucleation and in-situ nucleation in AA7050 aluminium alloy. *Acta Materialia*, **149**, 377-387.

[18] Chung, T. F., Yang, Y. L., Hsiao, C. N., Li, W. C., Huang, B. M., Tsao, C. S., Shi, Z., Lin, J., Fischione, P. E., Ohmura, T., & Yang, J. R. (2018). Morphological evolution of GP zones and nanometer-sized precipitates in the AA2050 aluminium alloy. *International Journal of Lightweight Materials and Manufacture*, **1**(3), 142-156.

[19] Marioara, C. D., Lefebvre, W., Andersen, S. J., & Friis, J. (2013). Atomic structure of hardening precipitates in an Al–Mg–Zn–Cu alloy determined by HAADF-STEM and first-principles calculations: Relation to η-$MgZn_2$. *Journal of Materials Science*, **48**(10), 3638-3651.

[20] Bendo, A., Matsuda, K., Lee, S., Nishimura, K., Nunomura, N., Toda, H., Yamaguchi, M., Tsuru, T., Hirayama, K., Shimizu, K., Gao, H., Ebihara, K., Itakura, M., Yoshida, T., & Murakami, S. (2017). Atomic scale HAADF-STEM study of η' and η_1 phases in peak-aged Al–Zn–Mg alloys. *Journal of Materials Science*, **53**(6), 4598-4611.

E.A. Fischione Instruments, Inc.
9003 Corporate Circle
Export, PA 15632 USA
Tel: +1 724.325.5444
Fax: +1 724.325.5443
info@fischione.com
www.fischione.com

Document Number AN025 Revision 00 07/2021